



City Research Online

City St George's, University of London

Citation: Mikulich, V., Nassauer, B., Kuna, M. & Brücker, C. (2015). Experimental and numerical study of interaction between particle loaded fluid and a rough wall with micropillars. *Tribology International*, 83(March), pp. 42-50. doi: 10.1016/j.triboint.2014.10.009

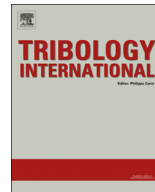
This is the accepted version of the paper.

This version of the publication may differ from the final published version. To cite this item please consult the publisher's version.

Permanent repository link: <https://openaccess.city.ac.uk/id/eprint/12979/>

Link to published version: <https://doi.org/10.1016/j.triboint.2014.10.009>

Copyright and Reuse: Copyright and Moral Rights remain with the author(s) and/or copyright holders. Copies of full items can be used for personal research or study, educational, or not-for-profit purposes without prior permission or charge, unless otherwise indicated, provided that the authors, title and full bibliographic details are credited, a hyperlink and/or URL is given for the original metadata page and the content is not changed in any way. For full details of reuse please refer to [City Research Online policy](#).



Experimental and numerical study of interaction between particle loaded fluid and a rough wall with micropillars

V. Mikulich*, B. Nassauer, M. Kuna, C. Brücker 

TU Bergakademie Freiberg, Institute of Mechanics and Fluid Dynamics, 09596 Freiberg, Germany

ARTICLE INFO

Article history:

Received 13 May 2014

Received in revised form

17 September 2014


Accepted 14 October 2014

Keywords:

Ring shear device

Particle–fluid interaction

Discrete element simulation

Abrasive slurry 

Micro-pillars

ABSTRACT

Experimental and numerical studies of the behavior of a slurry in a shear flow over a rough surface with a defined micro-structure are presented. A new ring shear device was built which contains an optically transparent test chamber. Its bottom wall contains arrays of micro-cantilever force sensors simulating a defined surface roughness created by deep-etching of micro-pillars in a silicon wafer. The results of visual observation of the interaction of the suspension with the structured surface during severe deformation are shown. Observations comprise the liquid phase motion, i.e., the interaction between the liquid phase and solid particles, the movement of separate particles and their interactions with the micro-pillars. Abrupt changes in rotational motion and translational velocity of particles are observed that induce mutual collisions and successive formation and break-up of cluster structures of various types. In addition to the experiments the process was simulated with discrete element (DEM) simulations. Many characteristics found in the experiments are reproduced by the simulations. Furthermore the physical quantities of the process like contact forces or velocities can be quantified which helps us to develop more detailed models of the abrasive behavior of slurries.

© 2014 Published by Elsevier Ltd.

1. Introduction

In many technical applications of material processing and process technology, such as grinding, lapping, and wire sawing, suspensions of abrasive particles and a carrier fluid (slurries) are used to cause the micro-mechanical removal and to ensure the transport of the removed material [1–3]. Here, the removal process happens in a narrow gap between the process tool and the workpiece surface. The complex mechanical behavior of abrasive particles in interaction with the walls and multiple contacts among each other in the process gap as well as cluster formation and break-up are not yet sufficiently understood [4,5]. Detailed visualizations of the dynamics on the local particle scale are difficult and therefore scarce. Hence, a more fundamental understanding of the process parameters that determine the final surface quality is still lacking.

This paper presents a new experimental reference-model for investigations of such processes in thin film flows, which is based on microscopic measurement techniques of the forces at particle–wall interaction as well as the flow behavior at the micro scale. The reference model has defined boundary conditions regarding the roughness and the fracture behavior of the surface which offers

unique possibilities for comparison and validation of the numerical simulations. Such simulations of the process are performed using discrete element method (DEM) [6]. This method allows for a description of the interaction of particles with the micro-pillars. Assuming laminar shear flow, the hydrodynamic forces are taken into account by evaluating Stokes' friction law. The motion of the particles as well as the interaction forces and the fracture events of pillars can be simulated for larger number of particles that allows us to gain a statistical description of the abrasion process.

2. Experimental details

Up to now, measurements of shearing behavior of granular materials have been carried out in different types of ring shear testers as discussed in [7–10]. The present study was carried out using a new ring shear device that contains an optically transparent test chamber which allows observing the slurry motion as well as the particle–wall contact forces. The narrow test chamber is defined by the outer edges of a glass ring as shown in Fig. 1. The inner and the outer diameter of the ring are 100 mm and 120 mm, respectively. The slurry is held in the gap between the upper glass ring and the fixed bottom wall. Shear is imposed by rotation of the upper ring under defined axial load and rotation speed. The bottom wall represents the micro-structured surface used for the

* Corresponding author.

E-mail address: vladimir.mikulich@imfd.tu-freiberg.de (V. Mikulich).

Nomenclature

M_b	bending moment
F_q	transversal shear force
q	distributed load
ρ	curvature
ϕ	inclination of the beam
γ	shear strain
u	deflection of the beam
E	Young's modulus
G	shear modulus
ν	Poisson's ration
I	moment of inertia

A	area of the cross section
l	length of the beam
F^A, F^B	forces acting on the particles
M^A, M^B	moments acting on the particles
n_i^A, n_i^B	tangent direction of the beam at point A and B
r_i^{AB}	vector from A to B
d	damage variable with $0 < d < 1$
σ^{c0}	initial strength
σ^c	current residual strength
σ^*	equivalent stress
σ^d	stress of the damaged beam
η	viscosity of the fluid
$\dot{\gamma}$	shear rate of the fluid

analysis of deformation, damage and wear in industrial silicon processing, see Fig. 2. The surface pattern was created by etching slender micro-pillars that are intended for simulating a defined wall roughness with poroelastic behavior in wall-parallel direction. At the same time the pillars serve as force sensors of the type of micro-cantilever beam according to the measurement principle described in [11,12]. The deformation and the fracture of the micro-pillars during interaction with the particles in the suspension are detected by imaging from the top and side walls. Brücker et al. [11] and Brücker [12] used such an array of flexible micro-hairs in the form of small slender micro-pillars made from an elastomer to measure the wall friction force distribution in turbulent flows. The same principle is applied herein to measure the contact forces during interaction of the particles with the walls.

The slurry consisted of a mixture of glycerine as fluid phase and glass balls with a diameter of 400–750 μm , coated with fluorescent material. Glass balls differ only in size. For flow studies, small fluorescent tracer particles with a diameter of 20 μm were also added. To study how the shape of particles affects their motion, the slurry contained a few particles consisting of two or three spheres glued together. The volume concentration of the solid phase varied between 10% and 20%. The thickness of the slurry layer was varied in experiments and was adjusted typically to 2–3 diameters of the glass balls. The experimental results which are presented here were carried out at a shear rate of $\dot{\gamma} = 2 \text{ s}^{-1}$ and a slurry layer thickness of 1.5 mm. The slurry behavior during shear loading was observed with CCD cameras from two sides of the flow chamber. The video recordings were taken a considerable large time after starting the shear cell. Light emitting diodes provided illumination and dye filters ensured epifluorescent imaging. The liquid phase motion and its interaction with large particles were studied with the small-sized

tracer particles. Bending of the micro-pillars was detected by the reflections at the tip of the cantilever beams.

3. Experimental results and discussion

The optical access into the slurry gap allows the observation of particle behavior in the suspension, the interaction between the liquid phase and particles, the movement of separate particles, their mutual interaction and the interaction with the micro-structured surface.

We have observed a variety of typical motion patterns many of which can be seen on the photographs shown in Fig. 3, which are described in the following. From a large sequence of images an excerpt of eight successive pictures is shown at a fixed spatial observation frame. In the pictures it is possible to watch the position of the numbered glass balls over the time. Furthermore, one can see the tips of the micro-pillars and some of them being broken and moving with the fluid. During shear loading of the slurry liquid phase, all particles (glass balls) in the solid phase start moving from the initial state. Due to the velocity gradient, all particles also come into rotation. Thanks to the uneven coating of the glass balls, we could not only determine the translational motion but also quantify particle rotation in the images. Moving speed and rotation speed of particles being not in contact with other particles depend on their size (diameter) and their position in the layer of a sheared suspension. The position of the particles could be estimated from the simultaneous recordings from the side view. Therein we could identify the particles and their position in the gap.

The translational speed of most of the particles coincides with the local velocity of the liquid phase. The translational motion of both is observed from the video recordings and the horizontal velocity along the shear direction was roughly the same for the particles when freely floating (without contact) and the fluid in the shear flow, thus particles closer to the upper wall move faster than particles near the bottom wall. The fluid density (glycerol) is 1263 gs m^{-3} , the density of the glass balls is 2.5 gs m^{-3} . Thus there is a small vertical settling velocity of the particles which however is two order of magnitude lower than the mean translational velocity. For example, the particles #39 (Fig. 3f, g) and #28 (Fig. 3e, f) which are moving in a layer of liquid closer to the rotating ring move faster in comparison to other particles. The speed of rotation relative to the translational speed of the particles increases when the particles came into contact with the tips of the micro-pillars. Figs. 4 and 5 show an example of the interaction the ball with a structured surface by means of the temporal evolution of translational and wall-normal coordinates of the ball as well as the ball rotation. Due to collisions with other particles the ball

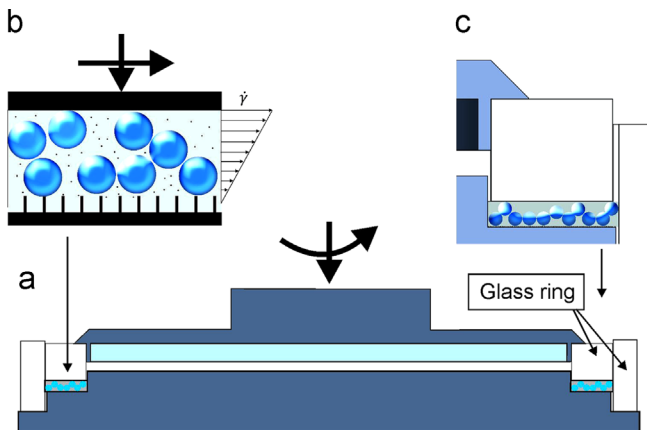


Fig. 1. Schematic of the sample chamber.

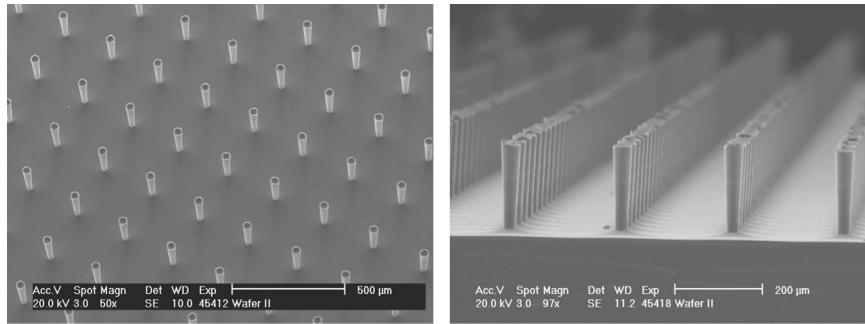


Fig. 2. Scanning electron microscope image of a micro-pillar array.

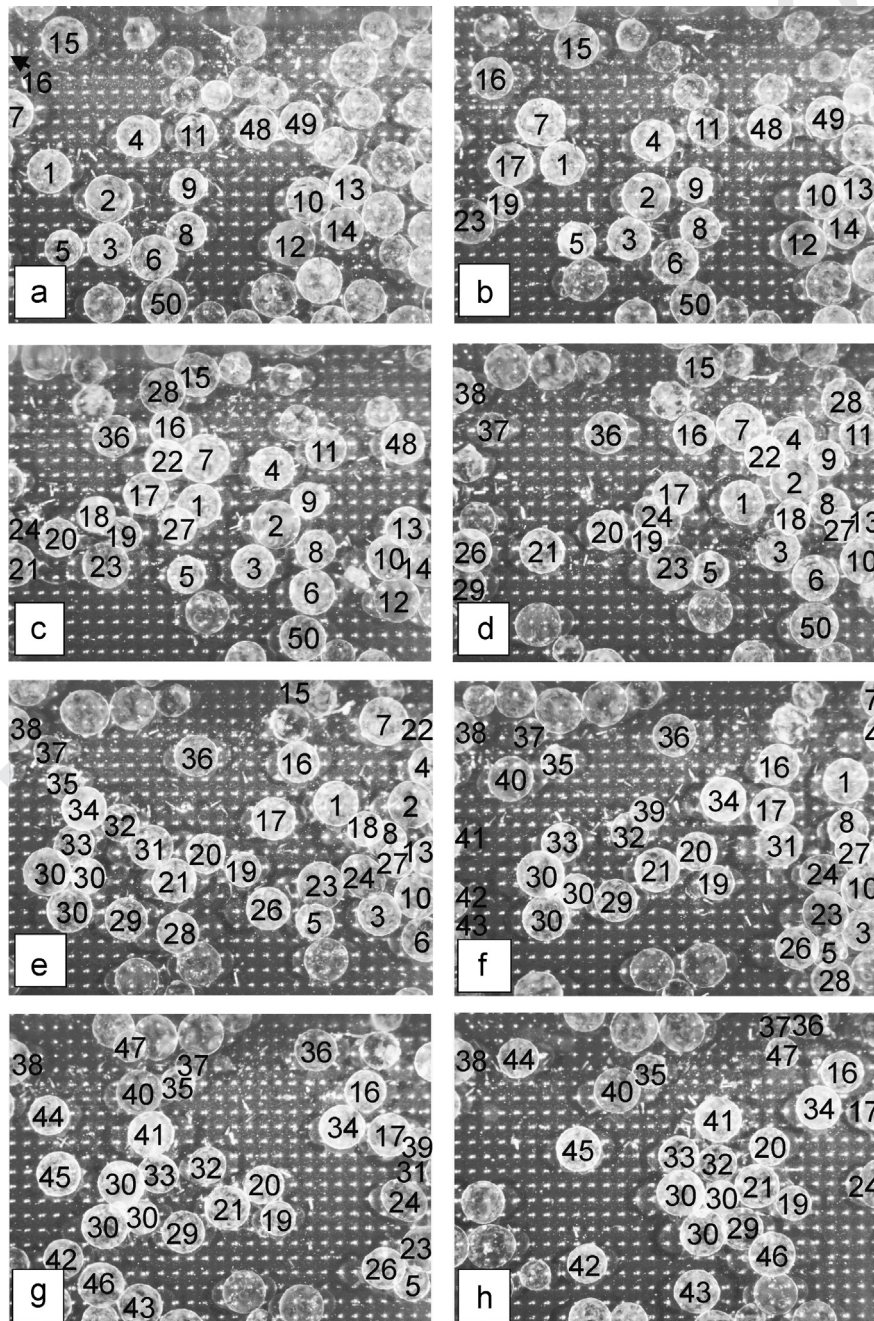


Fig. 3. Image sequence showing the particle motion in the suspension under shear load of the slurry (flow is from left to right). Recorded with 12 fps at 1600×1200 px². The figure shows every twelfth picture.

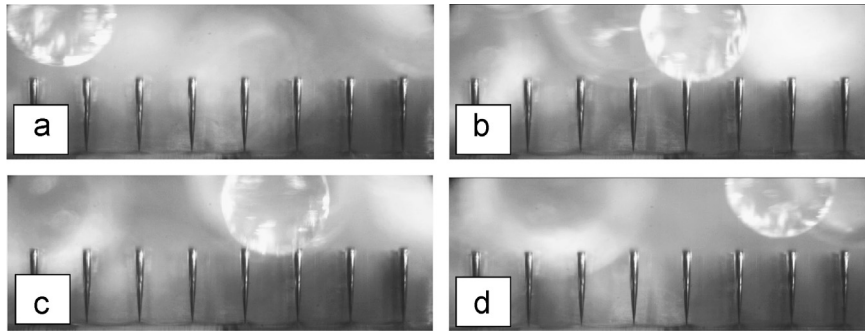


Fig. 4. Image sequence showing the particle position at different times after the beginning of the video recording at (a) 60 ms; (b) 236 ms; (c) 296 ms and (d) 384 ms.

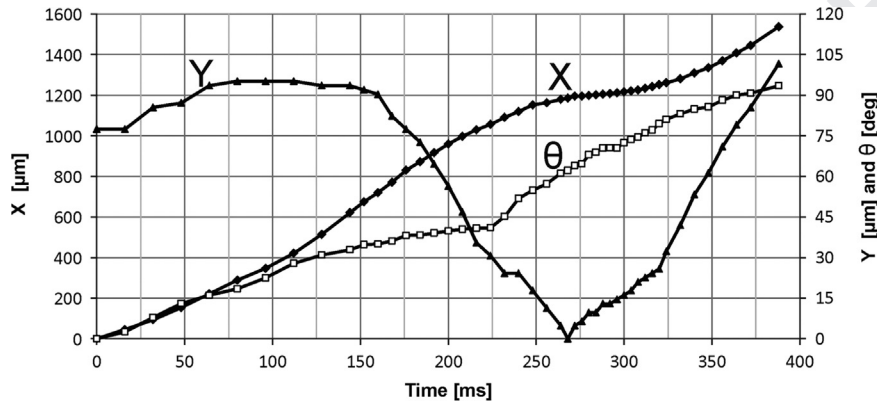


Fig. 5. The temporal evolution of translational coordinate X and wall-normal coordinate Y of the ball as well as the ball rotation θ (Fig. 4).

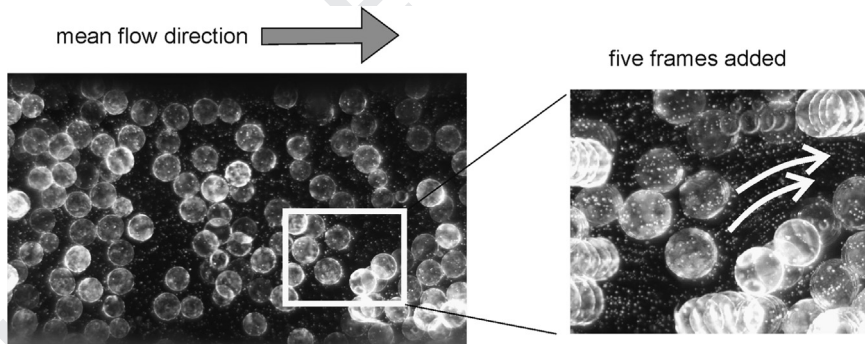


Fig. 6. Visualization of local flow around an attached clusters with multi-exposure method.

changes its direction – it first moves to the bottom. When it gets into contact with the pillar, the rate of translational motion is slowed down, and the rotational speed increases. Then, the ball moves upwards due to the repulsive forces.

In addition, the direction of movement of the liquid phase has impact on the path of the movement of single particles. As an example it is possible to watch the motion of particle #37 (Fig. 3d, e, f) and particle #44 (Fig. 3g, h) with the liquid phase around a particle #38 which is slower than the others. This effect can also be seen in Fig. 6 where individual particles flow around a large cluster.

In Fig. 3 it is also demonstrated that, at a shear flow in a thin layer, many particles of the suspension, even at relatively low concentrations, cannot move independently. Due to the kinematic restrictions of the test chamber walls, their roughness (microstructures) affects strongly the behavior of particles. It is manifested by abrupt changes in the motion direction, translational and rotational speed of the particles when the particles came in contact with the micro-pillars. In these cases, we observed a

definite discrepancy between the velocities of the liquid layer and the particles. The individual changes in rotation direction and translational velocity of particles after wall contact induce the formation of clusters or aggregate structures of various types. The particles form differently oriented chains and compact structures of different densities. These aggregate structures sometimes can remain for longer periods and continue to move as a unit. On the other hand, the clusters can again disintegrate after impact with other individual particles or contact with the bottom wall.

The particles consisting of two or three glued balls behave radically unlike from simple balls. The hydrodynamic forces that arise in a flow lead to orientation of an asymmetric particle relative to the streamlines. Because of the small thickness of the layer of sheared suspension, rotation of such particles is partially limited. They decelerate typically more often and they tend to attach to the bottom wall and remain at rest. Their rotation is typically more complicated and periodical. In Fig. 3e–h, we can observe the motion of a larger particle agglomerate (glued from three balls) as particle #30.

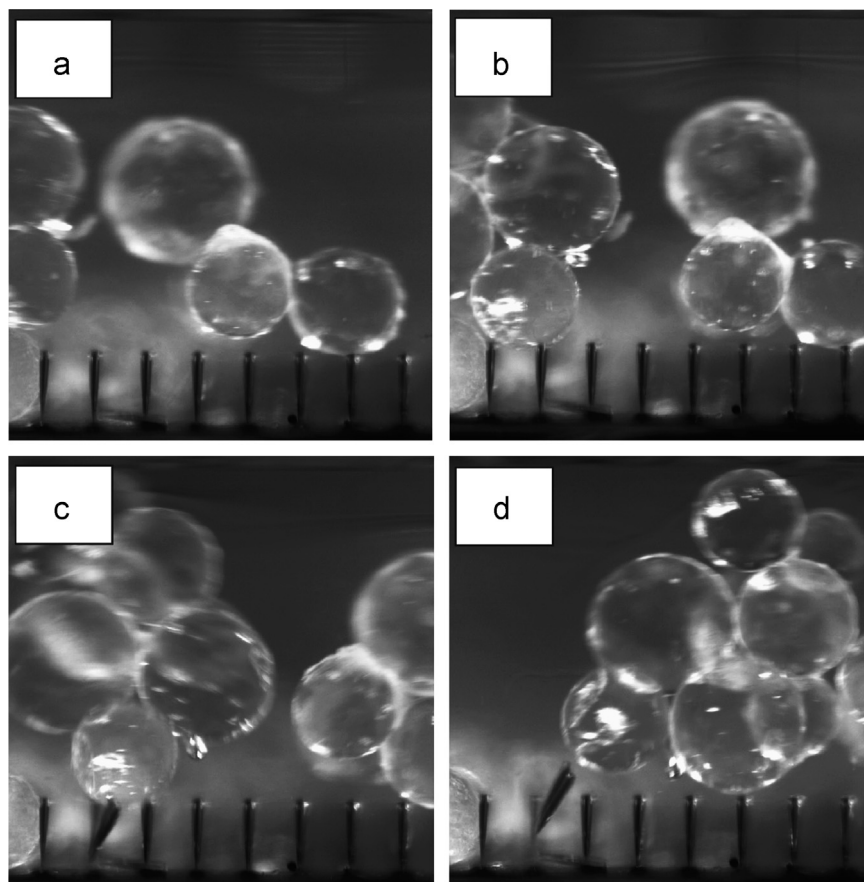


Fig. 7. Interaction of particles with the micro-pillar surfaces.

The interaction of particles with the bottom surface is indicated by the abrupt deceleration of movement and the tendency to stop. As soon as a particle remains in contact with a micro-pillar and stops its motion, it prevents the free flow of other trailing particles and leads to structure formation. Movement of particles #13 and #10 in Fig. 3 is an example of such behavior. After deceleration and coming to rest, subsequent movement of large particles or aggregates then causes high hydrodynamic drag forces and drastically enlarges the contact forces at the micro-pillar. This eventually leads to the fracture of the micro-pillars in a defined manner, compare Fig. 7.

For balls #37, #38 the motion is affected by the gaps in the micropillar forest that has been formed after individual fracture. Fracture of rods leads to a change in the structure of the surface, which affects the nature of the movement of balls. Once the balls have entered these gaps they are trapped and their velocity is reduced to zero (jamming, see Fig. 3d–f). This often leads to the formation of clusters and a subsequent acceleration of the destruction of the rods and then the balls start again to flow.

4. Numerical simulation of the shear flow

In addition to the experiment the particle motion was also simulated by means of the discrete element method (DEM). The fundamentals of this method are described in [13]. In order to take into account the slightly irregular shape of the coated glass spheres, icosahedra are chosen as particle geometry. The adopted special DEM approach has been developed in [14,15]. The fluid flow is assumed to be a laminar plane Couette flow, which certainly is a first approximation for this multiphase system. The

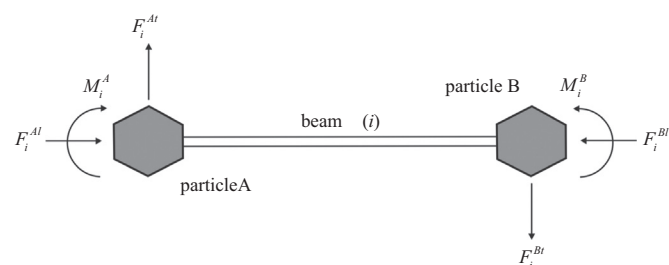


Fig. 8. Sketch of the micro-pillar model: Timoshenko beam with two particles at its ends.

influence of the flow on the particle motion is taken into account by Stokes' friction forces. The reverse feedback of the particle motion onto the fluid flow is neglected. The glass ring is modeled by a set of rigidly connected brick-shaped particles. This is a common technique in DEM to model rigid walls. It allows us to account for the mechanical interaction between the particles in the fluid and the glass ring. The glass ring respectively the wall particles move with a fixed velocity in linear direction. The simulation window has a size of 10 mm in the direction of the shear and 5 mm in the span direction. The conditions on the boundaries of the simulation window are assumed as periodic, i.e. particles running out at one side come in at the opposite boundary. The micro-pillars are modeled by two particles connected with a Timoshenko beam, see Fig. 8. The particle on the tip of the beam is able to move due to interaction with the slurry, while the other at the bottom wall is fixed in space. The Timoshenko beam model is described in Section 4.1.

4.1. Timoshenko beam model for DEM

4.1.1. General Timoshenko beam theory in 2D

The basic equations of Timoshenko beam theory [16] are as follows:

$$M_b = EI\rho \tag{1}$$

$$F_q = \kappa GA\gamma \tag{2}$$

$$F_q = M_b' \tag{3}$$

$$q = -F_q' \tag{4}$$

$$\rho = -\phi' \tag{5}$$

$$\gamma = u' - \phi \tag{6}$$

$$G = \frac{E}{2(1+\nu)} \tag{7}$$

M_b , F_q and q are the bending moment, the shear force and the distributed load, respectively. ρ , ϕ , γ and u are the curvature, the inclination, the shearing strain and the deflection, respectively. E , G , and ν are Young's modulus, the shear modulus and Poisson's ratio, respectively. I and A are the moment of inertia and the area of the cross section of the beam, respectively. κ is a correction factor for shear, which is defined as $\kappa = \frac{5}{6}$. Eqs. (1)–(6) lead to

$$\kappa GA(u' - \phi) + EI\phi'' = 0 \tag{8}$$

$$\kappa GA(u'' - \phi') = -q. \tag{9}$$

When this model is used in DEM, the distributed load q is zero and the deflection and angles at the ends of the beam are equivalent to those of the particles A and B attached to the beam:

$$q = 0 \tag{10}$$

$$u(0) = u^A \tag{11}$$

$$u(l) = u^B \tag{12}$$

$$\phi(0) = \phi^A \tag{13}$$

$$\phi(l) = \phi^B \tag{14}$$

l is the length of the beam. This leads to the internal force and moment:

$$F_q = \beta(u^B - u^A) - \frac{l}{2}\beta(\phi^B + \phi^A) \tag{15}$$

$$M_b(z) = \beta(u^B - u^A)\left(x - \frac{l}{2}\right) - \left(\frac{l}{2}\beta\left(x - \frac{l}{2}\right)\right)(\phi^B + \phi^A) + \frac{EI}{l}(\phi^A - \phi^B) \tag{16}$$

with

$$\beta = \frac{1}{\frac{l^3}{12EI} + \frac{l}{\kappa GA}} \tag{17}$$

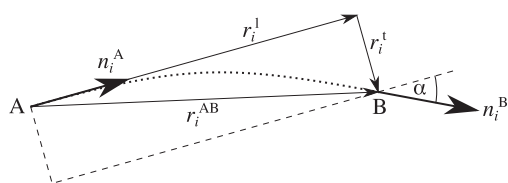


Fig. 9. Vectors for calculation of Timoshenko beam.

The forces and moment acting on the particles are

$$F^A = F_q \tag{18}$$

$$F^B = -F_q \tag{19}$$

$$M^A = M_b(z=0) \tag{20}$$

$$M^B = M_b(z=l) \tag{21}$$

4.1.2. Evaluation of the equations in 3D DEM

For the evaluation of the presented equations of a Timoshenko beam in a 3D DEM framework several vectors have to be defined. n_i^A and n_i^B define the tangent direction of the beam at points A and B, see Fig. 9. x_i^A and x_i^B are the coordinates of points A and B. r_i^{AB} is the vector from A to B:

$$r_i^{AB} = x_i^B - x_i^A \tag{22}$$

n_i^A is chosen as the principal direction of the beam. Then the distance between A and B can be described by a longitudinal component r_i^l and the transversal displacement of point B r_i^t :

$$r_i^l = (r_j^{AB} n_j^A) n_i^A \tag{23}$$

$$r_i^t = r_i^{AB} - r_i^l \tag{24}$$

As n_i^A was defined as the principal direction of the beam, the inclination at point A is $\phi^A = 0$. The inclination at point B is

$$\phi^B = \sin(\alpha) = |\epsilon_{ijk} n_j^B n_k^A|, \tag{25}$$

where α is the angle between n_i^A and n_i^B . Further a vector n_i^* is defined as

$$n_i^* = \frac{\epsilon_{ijk} n_j^B n_k^A}{\phi^B}, \tag{26}$$

which is directed perpendicular to the beam plane in Fig. 9. Then the transversal forces F_i^{At} and F_i^{Bt} and moments M_i^A and M_i^B acting on the particles can be calculated as

$$F_i^{At} = \beta r_i^t - \frac{l}{2}\beta\phi^B \frac{\epsilon_{ijk} n_j^A n_k^*}{|\epsilon_{ijk} n_j^A n_k^*|} \tag{27}$$

$$F_i^{Bt} = -\beta r_i^t + \frac{l}{2}\beta\phi^B \frac{\epsilon_{ijk} n_j^A n_k^*}{|\epsilon_{ijk} n_j^A n_k^*|} = -F_i^{At} \tag{28}$$

$$M_i^A = -\frac{l}{2}\beta |r_i^t| \frac{\epsilon_{ijk} r_j^t r_k^l}{|\epsilon_{ijk} r_j^t r_k^l|} + \left(\frac{l^2}{4}\beta - \frac{EI}{l}\right) \phi^B n_i^* \tag{29}$$

$$M_i^B = -\frac{l}{2}\beta |r_i^t| \frac{\epsilon_{ijk} r_j^t r_k^l}{|\epsilon_{ijk} r_j^t r_k^l|} + \left(\frac{l^2}{4}\beta + \frac{EI}{l}\right) \phi^B n_i^*. \tag{30}$$

Additionally the longitudinal forces F_i^{Al} and F_i^{Bl} are given as

$$F_i^{Al} = EA \frac{|r_i^l| - l}{l} n_i^A \tag{31}$$

$$F_i^{Bl} = -EA \frac{|r_i^l| - l}{l} n_i^A = -F_i^{Al}. \tag{32}$$

4.1.3. Damage model

In order to simulate pillar fracture a simple damage model is used that specifies the bearable load of the beam.

Then the forces and moments acting in the beam on the particles' sites are

$$F_i^{Ad} = (F_i^{At} + F_i^{Al})d \quad (33)$$

$$M_i^{Ad} = M_i^A d \quad (34)$$

$$F_i^{Bd} = (F_i^{Bt} + F_i^{Bl})d \quad (35)$$

$$M_i^{Bd} = M_i^B d, \quad (36)$$

where d is the damage variable with $0 < d < 1$. An undamaged beam has a damage variable of $d=1$, while $d=0$ resembles a completely failed beam.

In the following the evaluation of the current damage variable is described. In Fig. 10 the degradation of the relation between equivalent stress σ and equivalent strain ϵ with damage is illustrated. σ^{c0} is the initial strength. σ^c is the current residual strength with

$$\sigma^c = \sigma^{c0}d. \quad (37)$$

The nominal stress of the undamaged beam is

$$\sigma = \frac{|F_i^{Al}|}{A} + \frac{\max(|M_i^A|, |M_i^B|)}{I} r^p, \quad (38)$$

where r^p is the radius of the pillar cross section. The shear stress of the undamaged beam is

$$\tau = \frac{|F_i^{At}|}{A}. \quad (39)$$

The equivalent stress σ^* of the undamaged beam is calculated as

$$\sigma^* = \sqrt{\sigma^2 + 4\tau^2}. \quad (40)$$

The stress of the damaged beam is then

$$\sigma^d = \sigma^* d. \quad (41)$$

If the stress σ^d exceeds the residual strength σ^c damage occurs and the damage variable has to be updated. This is performed by finding the point, where the new stress is equivalent to the new residual strength while keeping the strain constant as illustrated in Fig. 10. The new residual strength σ^{cn} can be calculated as

$$\sigma^{cn} = \sigma^* - k(\sigma^* - \sigma^{c0}), \quad (42)$$

with

$$k = \frac{\epsilon^b}{\epsilon^b - \epsilon^a} \quad (43)$$

where ϵ^a is the equivalent strain where damage starts and ϵ^b is the equivalent strain where the beam breaks. The new value of the

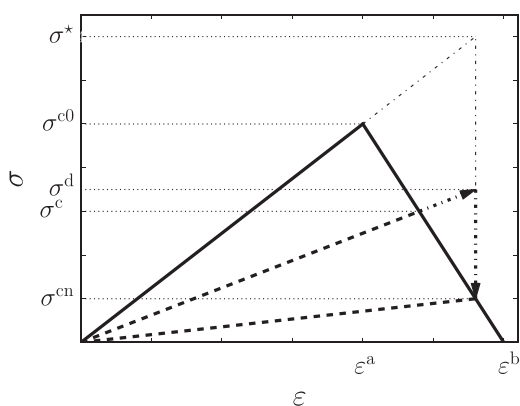


Fig. 10. Degradation of the σ - ϵ relation with damage.

damage variable is

$$d = \frac{\sigma^{cn}}{\sigma^*}. \quad (44)$$

Considering Hooke's law the above equations are equivalent to a reduction of Young's modulus due to damage:

$$\sigma^d = (Ed)\epsilon \quad (45)$$

The damage of the micropillars made from silicon is physically associated with the formation and evolution of microcracks in the pillars, which cause the degradation of the residual strength. This strength may be reduced by a high impact that breaks the micropillar immediately, or a slow degradation may occur under repeated loads which will finally lead to failure of the micropillars. Exactly this effect is to be reflected by our novel beam model combined with the damage mechanics approach. In addition, this approach also increases the numerical stability by providing a smooth transition between the undamaged and the completely failed stage of the beam.

5. Numerical simulation results

The simulations were carried out with Young's modulus of $E = 165$ GPa and Poisson's ratio of $\mu = 0.4$ for the micro-pillars, Young's modulus of $E = 70$ GPa and Poisson's ratio of $\mu = 0.3$ for the particles, and a viscosity of $\eta = 1.48$ Pas for the fluid. The shear rate is $\dot{\gamma} = 2 \text{ s}^{-1}$. In the first simulation we considered the non-central impact of a single particle against a pillar. The particle of diameter $600 \mu\text{m}$ moves in the fluid with a velocity v and strikes the pillar at a position, where the center of the particle is $260 \mu\text{m}$ above the top of the pillar. The development of velocity v and angular velocity ω is shown in Fig. 11. After collision, the velocity decreases for a moment and reaches later on its initial value due to acceleration by the fluid. On the contrary, the angular velocity of the particle is increased because of the experienced torque. Both phenomena could also be observed in the experiments. Furthermore it can be stated from the simulation results that the forces acting between a pillar and a single particle are too low to break the pillar.

In the further simulations the particle distributions (w.r.t. size and density) were chosen comparable to those in the experiments. First of all it was found that those particles not being in contact with other particles or pillars have a velocity equivalent to the local velocity of the fluid and rotate according to the shear rate. This behavior is quite obvious.

In Fig. 12 different physical properties of the particles in the shear flow are illustrated. The view is from the bottom. In the front are the pillars, in the back is the glass ring and in between are the

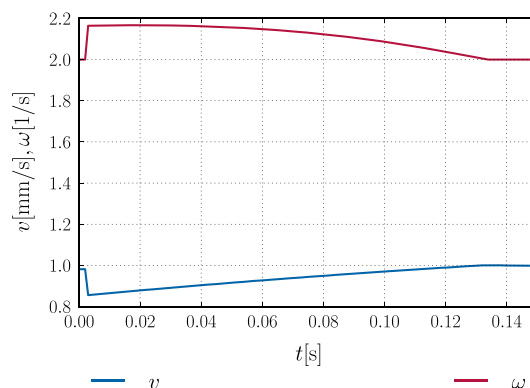


Fig. 11. Development of velocity v and angular velocity ω for particle colliding against pillar.

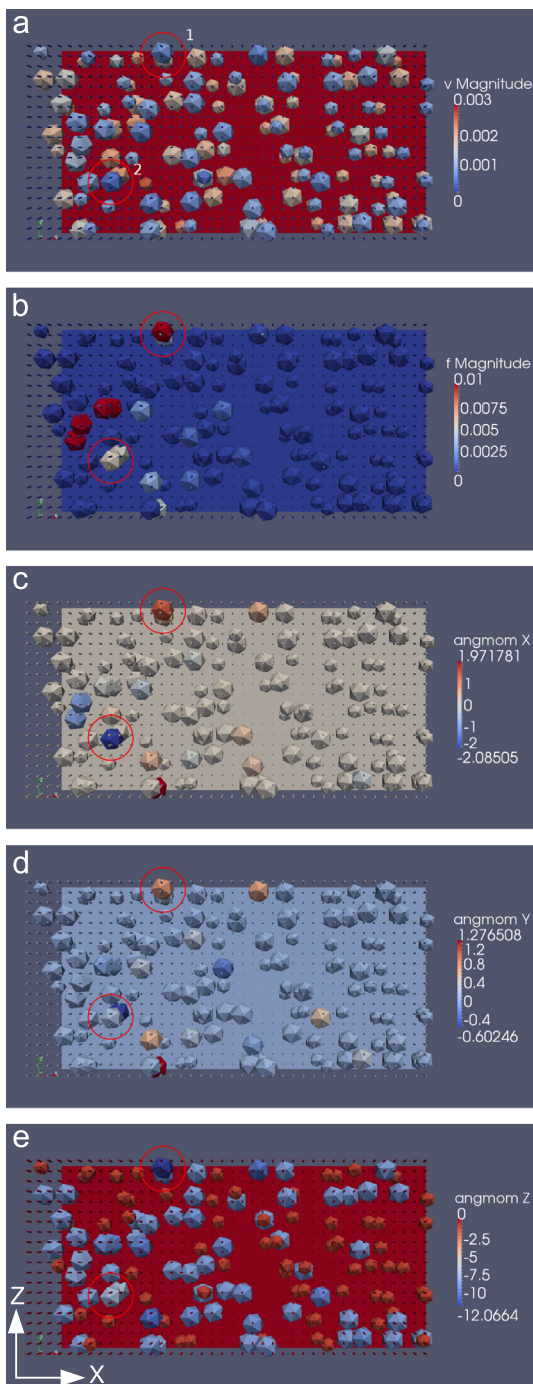


Fig. 12. Particle movement in the shear flow: The view is from the bottom. In the front are the pillars, in the back the glass ring and in between the particles. The flow is from left to right. The colored graphs show (a) velocity in m/s, (b) force in mN and (c, d) x, y and z component of angular momentum in mNs. (For interpretation of the references to color in this figure caption, the reader is referred to the web version of this paper.)

particles. A close look shall be taken on the constellations 1 and 2, where two particles and the pillars are interacting. A strong influence on the rotation can be observed. At position 1 the rotation around z (which is the rotation induced by the shear flow) of one particle increases, while at position 2 the rotation around z of both particles decreases. In both cases rotations around x and y can be observed. The simulation results have shown that rotations induced by contact are in the range of one-fifth of the rotation induced alone by the shear flow. The change of

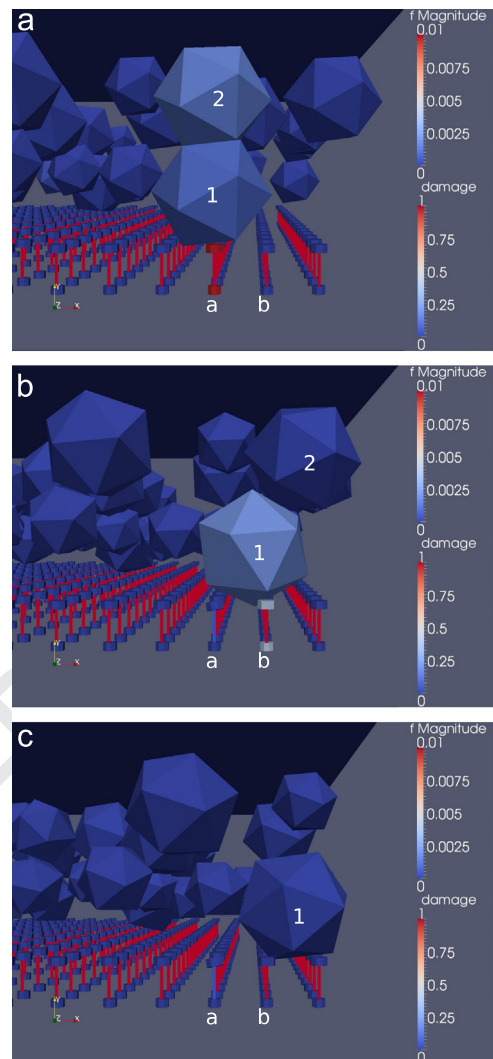


Fig. 13. Sequence with particles colored by force in mN and beams colored by damage variable. The time interval between A and B is 240 ms. The time interval between B and C is 210 ms. (For interpretation of the references to color in this figure caption, the reader is referred to the web version of this paper.)

the particle velocities induced by contact are in the range of one-tenth of the fluid velocity. In the experiment sideward movements of the particles can be observed which are induced by transversal flow of the fluid. This effect cannot be observed in the present simulation due to the simple model of the prescribed shear flow which does not take into account the feedback from particle interaction back onto the fluid (one-way coupling).

Fig. 13 shows three consecutive snapshots taken from a third simulation, where the pillars are modeled with Timoshenko beams. At time step A particles 1 and 2 and pillar 'a' are in contact. The high forces acting on the pillar due to the two particles lead to pillar breakage (pillar 'a' colored in blue in consecutive steps). In step B only particle 1 is in contact with pillar 'b'. The forces are too low to break the pillar (pillar 'b' colored in red in step C).

6. Conclusion

A new shear cell has been presented which allows the optical observation of cluster behavior and contact forces in a suspension. The new mechanical model is well suited for comparison with theoretical studies of abrasion due to the defined boundary conditions of micro-pillar bending and critical load when a

1 fracture happens. Our visual observations showed that during
 2 rotation, contact and structure formation, the flow around the
 3 particles creates largely different hydrodynamic forces which
 4 fluctuate in direction and magnitude. As a consequence flow
 5 patterns evolve which show micro-vortices resembling those that
 6 occur in locally turbulent flows. The largely fluctuating hydro-
 7 dynamic drag forces also cause critical loads that lead to fracture of
 8 the micro-pillars. These events were documented by live-pictures
 9 in the recordings and the broken micro-pillars that are flowing in
 10 the slurry after fracture.

11 The process has also been simulated by discrete element
 12 simulations. The results show good qualitative agreement with
 13 the experimental results, although some features cannot be
 14 reproduced yet due to the applied one-way coupling of the fluid
 15 with the structural motion. Thus, there is no feedback onto the
 16 shear flow by the motion of the particles and their mutual
 17 interaction. Nevertheless, the mechanical behavior shows already
 18 some of the typical features within the shear cell. When individual
 19 particles come into contact with the pillars, their movement is
 20 strongly influenced as observed in the experiments. The forces
 21 induced by a single particle in contact with a pillar are too low to
 22 induced pillar breakage. If an agglomerate of two particles comes
 23 into contact with a pillar, the contact forces are higher and pillar
 24 breakage can be observed in agreement with the observations in
 25 the experimental studies. This is attributed to the effect of the
 26 upper particle at higher flow speeds in the shear that pushes the
 27 pillar via the contact with the lower particle. Further work is
 28 needed to implement a full two-way coupling between the flow
 29 and the structural behavior to attribute also the effect of the
 30 cluster formation on the drag forces which is part of future work.
 31 This allows then the statistical analysis of fracture events in the
 32 cell under defined conditions parallel to long-term recordings of
 33 the fracture events in the experimental shear-cell. A comparison of
 34 both allows then a thorough and fundamentally sound modeling
 35 of the abrasive behavior of such slurries in machine processing.
 36
 37

Acknowledgments

The Deutsche Forschungsgemeinschaft (DFG) supported the work under Contract BR 1494/20-1 and KU 929/19-1.

References

- [1] Möller HJ. Wafering of silicon crystals. *Phys Status Solidi A Appl Mater Sci* 2006;203(4):659–69. 38
- [2] Bhagavat S, Liberato JC, Chung C, Kao I. Effects of mixed abrasive grits in slurries on free abrasive machining processes. *Int J Mach Tools Manuf* 2010;50(9):843–7. 39
- [3] Bidville A, Wasmer K, Michler J, Nasch PM, Van Der Meer M, Ballif C. Mechanisms of wafer sawing and impact on wafer properties. *Prog Photovolt: Res Appl* 2010;18(8):563–72. 40
- [4] Pei Z, Fisher G, Liu J. Grinding of silicon wafers: a review from historical perspectives. *Int J Mach Tools Manuf* 2008;48(12–13):1297–307. 41
- [5] Möller HJ. Basic mechanisms and models of multi-wire sawing. *Adv Eng Mater* 2004;6(7):501–13. 42
- [6] Bicanic N. *Discrete Element Method*. In: Hughes Encyclopedia of Computational Mechanics, vol. 1. Wiley; 2004. 43
- [7] Bjerrum L, Landva A. Direct simple-shear tests on a norwegian quick clay. *Geotechnique* 1966;16(1):1–20. 44
- [8] Bishop A, Green G, Garga V, Andresen A, Brown JD. A new ring shear apparatus and its application to the measurement of residual strength. *Geotechnique* 1971;21(2):273–328. 45
- [9] Bromhead E. A simple ring shear apparatus. *Ground Eng* 1979;12(5):40–4. 46
- [10] Carr JF, Walker DM. An annular shear cell for granular materials. *Powder Technol* 1968;1(6):369–73. 47
- [11] Brücker C, Spatz J, Schröder W. Feasibility study of wall shear stress imaging using microstructured surfaces with flexible micropillars. *Exp Fluids* 2005;39(2):464–74. 48
- [12] Brücker C. Signature of varicose wave packets in the viscous sublayer. *Phys Fluids* 2008;20(6). 49
- [13] Radjai F, Dubois F. *Discrete Element Modeling of Granular Materials*. Wiley & Sons; 2011 ISBN 9781848212602. 50
- [14] Nassauer B, Liedke T, Kuna M. Polyhedral particles for the discrete element method: geometry representation, contact detection and particle generation. *Granul Matter* 2013;15(1):85–93. 51
- [15] Nassauer B, Kuna M. Contact forces of polyhedral particles in discrete element method. *Granul Matter* 2013;15(3):349–55. 52
- [16] Timoshenko S. LXVI. On the correction for shear of the differential equation for transverse vibrations of prismatic bars. *Philos Mag Ser 6* 1921;41(245):744–6. 53